Supporting Information

Single-Phase Proton- and Electron-Conducting Ag-Organic Coordination Polymers for Efficient CO_2 Electroreduction

Yingbing Zou,[a,b] Tingting Zhan,[a] Ying Yang,[a] Zhiwen Fan,[a] Yunbin Li,[a] Yongfan Zhang,[c] Xiuling Ma,[*,a] Qianhuo Chen,[*,a,b] Shengchang Xiang,[a] Zhangjing Zhang,[*,a]

[a]*Fujian Provincial Key Laboratory of Polymer Materials, College of Chemistry and Materials science, Fujian Normal University，FuZhou, China,* 350007

[b]*Fujian Key Laboratory of Pollution Control & Resource Reuse, College of Environmental Science and Engineering, Fujian Normal University，FuZhou, China,* 350007

[c]*State Key Laboratory of Photocatalysis on Energy and Environment, College of Chemistry, Fuzhou University, Fuzhou, China, 350002*

Experimental Section

Materials and Instrumentation

All reagents were commercially available and used without further purification. Silver(I) nitrate ($AgNO_3$, AR), 1H-1,2,3-triazole (Tz, AR),1H-benzotriazole (Btz, AR), Sodium hydroxide (NaOH, AR) and Ethanol (EtOH, AR) were purchased from Sinopharm Chemical Reagent Co., Ltd. Powder X-ray diffraction (PXRD) were obtained on a Rigaku MiniFlex II powder diffractometer equipped with a Cu sealed tube (λ = 1.541874 Å) at 40 kV and 40 mA over the 2θ range of 5-30°. The simulated PXRD pattern was produced by using the Mercury V1.4 program and single-crystal diffraction data. Fourier transform infrared spectra (FT-IR, KBr pellet) were measured in the range of 400-4000 cm^{-1} by a Nicolet 5700 FT-IR. A Micromeritics ASAP 2020 surface area analyzer was used to measure the gas adsorption. The thermogravimetric analyses (TGA) were performed on a METTLER TGA/ STDA 851 thermal analyzer from 30 to 600 ℃ at a heating rate of 10 ℃/min under N_2 flow. The morphologies of the samples were characterized by Scanning Electron Microscope (SEM, Hitachi S-4800 scanning electron microscope). Elemental analytical (C, H, N) data were obtained on a PerkinElmer model 240C elemental analyzer. Electrochemical test data were recorded with a Versa STAT 3F (Princeton Instruments, USA). Electronic conductivity was evaluated by the measurement of I−V curves at the probe station with a Keithley 4200 semiconductor characterization system in voltage-sweeping mode.

Syntheses of Ag-MOCP-Tz and Ag-MOCP-Btz

Ag-MOCP-Tz were synthesized by a solvothermal method, with details as follows: $AgNO_3$ (0.17 g, 1 mmol) and Tz (0.083 g, 1 mmol) were dissolved in a mixture of EtOH (8 mL) and distilled water (4 mL), then heated at 100 ℃ for 24 h in a Teflon-lined steel bomb. The colorless rod-shaped crystals were obtained, washed with EtOH and dried at room temperature with a yield of 68 % (based on Ag). Elemental analysis—Found (theory): C=10.63 (9.96), H=0.74 (0.76), N=19.79 (18.77).

The synthesis of Ag-MOCP-Btz was according to a reported work.[1] 2.43 g BTZ was dissolved in 100 mL H_2O containing 0.76 g NaOH. 3.45 g/L $AgNO_3$ aqueous solution was added into the above BTZ solution. And white precipitate was immediately noted. Then the mixture was stirred for 30 min, filtered, re-dispersed in water, stirred 15 min, filtered, and air-dried, with a yield of 87% (based on Ag). Elemental analysis—Found (theory): C=32.39 (31.86), H=1.53 (1.78), N=17.93 (18.54).

Single Crystal X-Ray Diffraction (SCXRD) Studies

Data collection and structural analysis of crystal Ag-MOCP-Tz was performed on an Agilent Technologies SuperNova single crystal diffractometer equipped with graphite monochromatic Mo Kα radiation (λ = 0.71073 A). The crystal was kept at 293 K during data collection. By use of Olex2, the structure was solved with the Superflip structure solution program and refined with the ShelXL refinement package by using least-squares minimization. All nonhydrogen atoms were refined with anisotropic displacement parameters. The hydrogen atoms on the ligands were placed in idealized positions and refined by using a riding model. We employed PLATON and SQUEEZE to calculate the diffraction contribution of the solvent molecules and thereby produce a set of solvent-free diffraction intensities. The final formulas of Ag-MOCP-Tz were determined by the combination of elemental analysis. The detailed crystallographic data and structure refinement parameters for the compound of Ag-MOCP-Tz are summarized in Tables S1. (CCDC 2069516)

Electrical Performance Test

Electronic conductivity test

The conductivity of Ag-MOCP-Tz and Ag-MOCP-Btz was performed on pelletized samples pressed in a cylindrical die at about 0.26 t for 5 min to prevent sample decomposition from the high temperature. The lengths of Ag-MOCP-Tz measured by vernier calipers were recorded as 0.1 cm

and Ag-MOCP-Btz was 0.09 cm. Direct current two terminal method were investigated its conductivity with an input voltage -5 to 5 V and a sweep rate of 5 mV/s.

Proton conductivity test

Similar as electronic conductivity test, pelletized samples pressed in a cylindrical die at about 0.26 t for 5 min to prevent sample decomposition from the high temperature. The length records of Ag-MOCP-Tz and Ag-MOCP-Btz measured with vernier calipers are both 0.08 cm. AC impedance analysis was performed on the pellets using a two-probe method with a Solartron SI 1260 impedance/gain-phase analyzer and a 1296 dielectric interface impedance analyzer from 10 MHz to 100 Hz with an input voltage 100 mV. Humidity and temperature were controlled by using a XK-CTS80Z humidity control chamber. The conductivities at each temperature were measured after equilibration for a period of 30 min. The resistance value was determined from equivalent circuit fits of the first semicircle using ZView software. The proton conductivity was calculated via the following equation:

$$\sigma = \frac{l}{RS}$$

where l and S are the length (cm) and cross-sectional area (cm^2) of the samples, respectively, and R, which was extracted directly from the impedance plots, is the bulk resistance of the sample (V). The activation energy (Ea) for the materials conductivity was estimated from the following equation:

$$\sigma T = \sigma_0 \exp(-\frac{E_a}{K_B T})$$

where σ is the proton conductivity, σ_0 is the preexponential factor, k_B is the Boltzmann constant, and T is the temperature.

Electrochemical Measurements

Preparation of working electrodes

2.6 mg of Ag-MOCP-Tz powder were dispersed in a solution containing isopropanol (0.7 mL), H_2O (0.2 mL) and 5 wt% Nafion solution (0.1 mL) with ultrasonic treatment for 30 min. Then, all of the catalyst ink was sprayed onto the two sides of a carbon paper (CP) with a size of 1.0×1.0 cm^2 to get the mass loading of 2.0 $mg \cdot cm^{-2}$ (30% loss) and then dried at 80 ℃. Ag-MOCP-Btz modified electrodes were also prepared in the same manner.

Electrocatalytic CO_2 reduction.

All the electrochemical measurements were conducted on a proton exchange membrane (Nafion 117) separated H-type electrochemical cell connected to an electrochemical workstation (Versa STAT 3F, Princeton Instruments, USA), and on the traditional three-electrode system with a Ag/AgCl electrode and platinum mesh as reference and counter electrodes, respectively. CO_2-saturated 0.5 mol L^{-1} $KHCO_3$ (pH = 7.2) was used as electrolyte. CO_2 with a flow rate of 20.0 mL min^{-1} was through the electrolyte during electrolysis. All the measured potentials were converted to Reversible Hydrogen Electrode (RHE). And the electrochemical data were obtained without iR compensation. The linear sweep voltammetry (LSV)was performed at the applied voltage of 0 to -2.5 V (vs. Ag/AgCl) and a sweep rate of 5 mV/s. Tafel slopes were calculated based on the LSV curves by plotting potential against log (j_{CO}). The electrochemical impedance spectroscopy (EIS) was recorded at -0.28 to -0.78 V vs. RHE with the frequency ranging from 0.1 Hz to 10^5 Hz at the AC amplitude of 10 mV. I-t curves was electrolysis for 3600s at each selected potential

The detection process of gas products is to perform a constant potential test first. After controlling potential electrolysis for 10 min, the gas-phase composition was analyzed by an online gas chromatograph (PANNA, A60, China) with a flame ionization detector (for detecting CO) and thermal conductivity detector (for detecting H_2). The corresponding FEs of the gas products were calculated on the basis of the following equation:

$$FE = \frac{v \times 10^{-6} \times V_{co_2} \times 10^{-6} \times 96485.3 \times n \times 101300}{8.314 \times 298.15 \times i \times 60}$$

where V_{CO2} is the flow rate of CO_2 (20 mL min^{-1}), v (ppm) is the concentration of the gas-phase products including CO and H_2, n is the quantity of transferred electrons for producing CO or H_2, and i (A) is the cell current at a steady state.

The liquid products were measured using NMR (Bruker 400 MHz, Switzerland) spectroscopy. According to the number of electrons that need to be transferred to produce one molecule liquid product, the FE can be calculated as follows：

$$FE = \frac{96485.3 \times n \times V \times C_i}{Q}$$

where V is the electrolyte liquid volume, n is the number of electrons used for producing one molecule liquid product, C_i is the concentration of liquid product and Q (A s) is the total quantity of electric charge.

The TOF for CO generation was calculated as following (Elapsed time for 1 h)[2]

$$TOF = \frac{I_{co} \times 3600}{n \times 96485.3} / \frac{m_{cat} \times w\%}{M_{Ag}}$$

m_{cat}: Catalyst mass in the carbon paper (g), $w\%$: Ag weight ratio loading in the catalyst (SCXRD analysis results), M_{Ag}: Atomic mass of Ag (107.87 g mol^{-1}), I_{CO}: Partial CO current, n: The number of electrons transferred for CO formation.

Density functional theory calculation details.

First-principle Density functional theory (DFT) calculations were carried out using the plane-wave technique with exchange correlation interactions modeled by GGA-PBE functional,[3] as implemented in the VASP code.[4] The ion-electron interactions were described by the projector-augmented plane-wave approach. A plane-wave cutoff energy of 400 eV was used in all calculations. The Monkhorst-Pack k-point grid (1×1×1) was used to sample the Brillouin zone of surface. The convergence thresholds of energy and forces were set as 1×10^{-5} eV and 0.02 eV $Å^{-1}$, respectively. The ground state structures of *COOH and *CO adsorbed on the catalyst surfaces were determined by searching all the possible configurations on possible active sites till found that of lowest energy without considering the solvation effects. The free energy of the adsorbed state was calculated as:[5]

$$\mathbf{G = E + E_{ZPE} - TS + \int CpdT}$$

where T is the temperature, E is the electronic energy calculated by DFT; E_{ZPE} and Sare the zero point energy and entropy, respectively, estimated under harmonic approximation from the frequency analysis. The ∫CpdT is small for the adsorbates compared to E and E_{ZPE}, which can be neglected in this study.

Fourier Transform Infrared (FT-IR) spectrums test

FT-IR spectrums of Ag-MOCP-Tz and Ag-MOCP-Btz are displayed in Figure S3. It shows C-N stretching vibration at 1093 cm^{-1} for the compound Ag-MOCP-Tz (Figure S3a). While, the C-N stretching vibration peak in Ag-MOCP-Btz appears at 1120 cm^{-1} (Figure S3b). The peak at 3050 cm^{-1} and the peak near 1480 cm^{-1} belonged to the C-H characteristic peak and the C=C stretching vibration on the benzene ring respectively in the spectrums of Ag-MOCP-Btz. Based on the above results, Ag-MOCP-Tz and Ag-MOCP-Btz contain related functional groups of Tz and Btz, respectively.

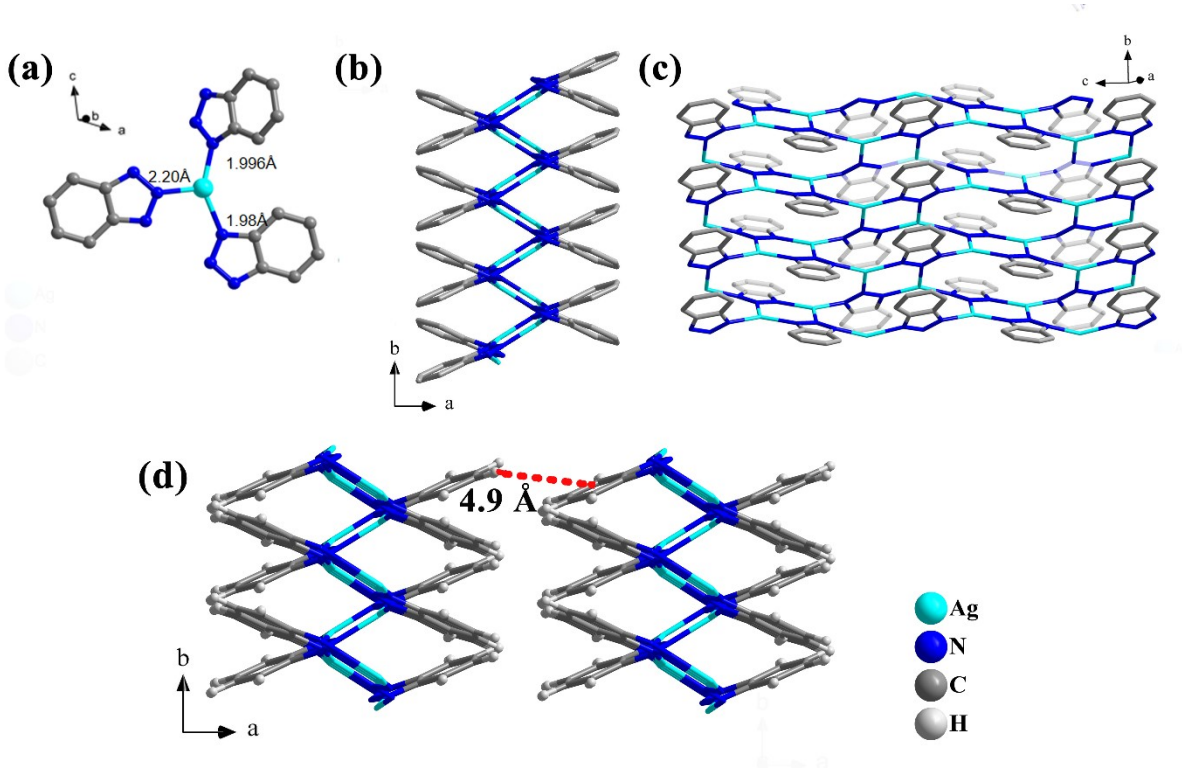

Figure S1. (a) Ball-and-stick diagram of the crystal structure of Ag-MOCP-Btz and its coordination method with Ag(I) and Btz, (b) The 2D layer of Ag-MOCP-Btz (constructed with Btz and the Ag(I)) along the direction of c-axis, (c) Single-layer structure along the *bc* plane of Ag-MOCP-Btz, (d) Structure by close packing of Ag-MOCP-Btz and the distance of H atoms in Btz to the other Btz centroids.

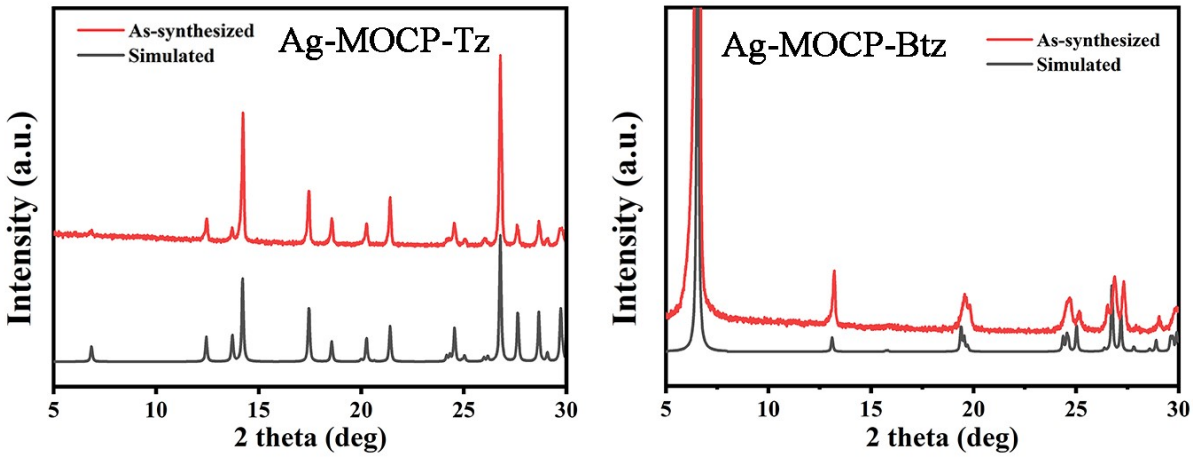

Figure S2. The powder XRD patterns of (a) Ag-MOCP-Tz and (b) Ag-MOCP-Btz.

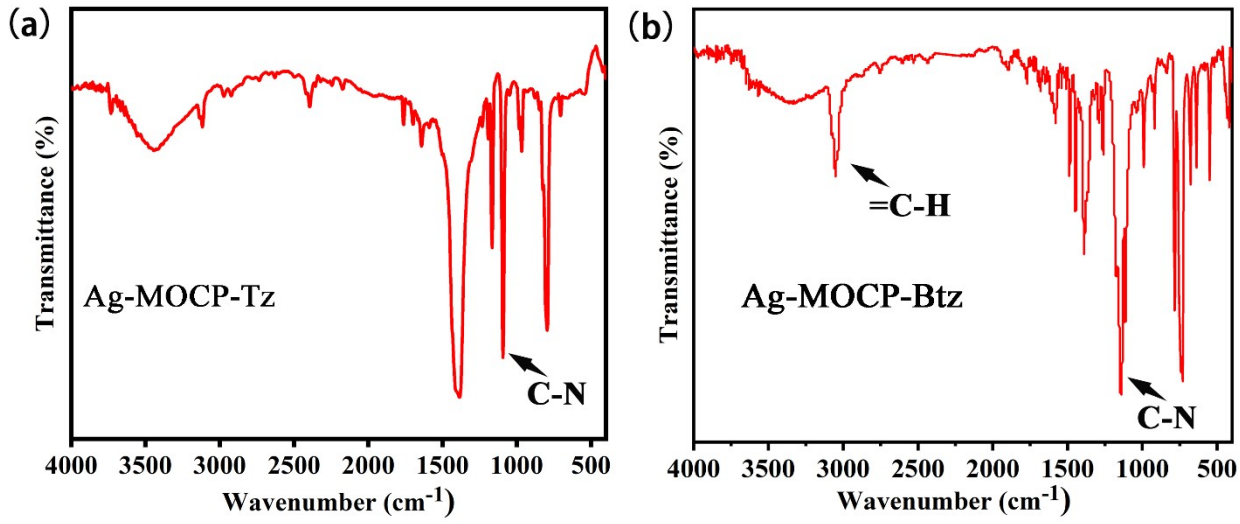

Figure S3. The FT-IR spectra of (a) Ag-MOCP-Tz and (b) Ag-MOCP-Btz.

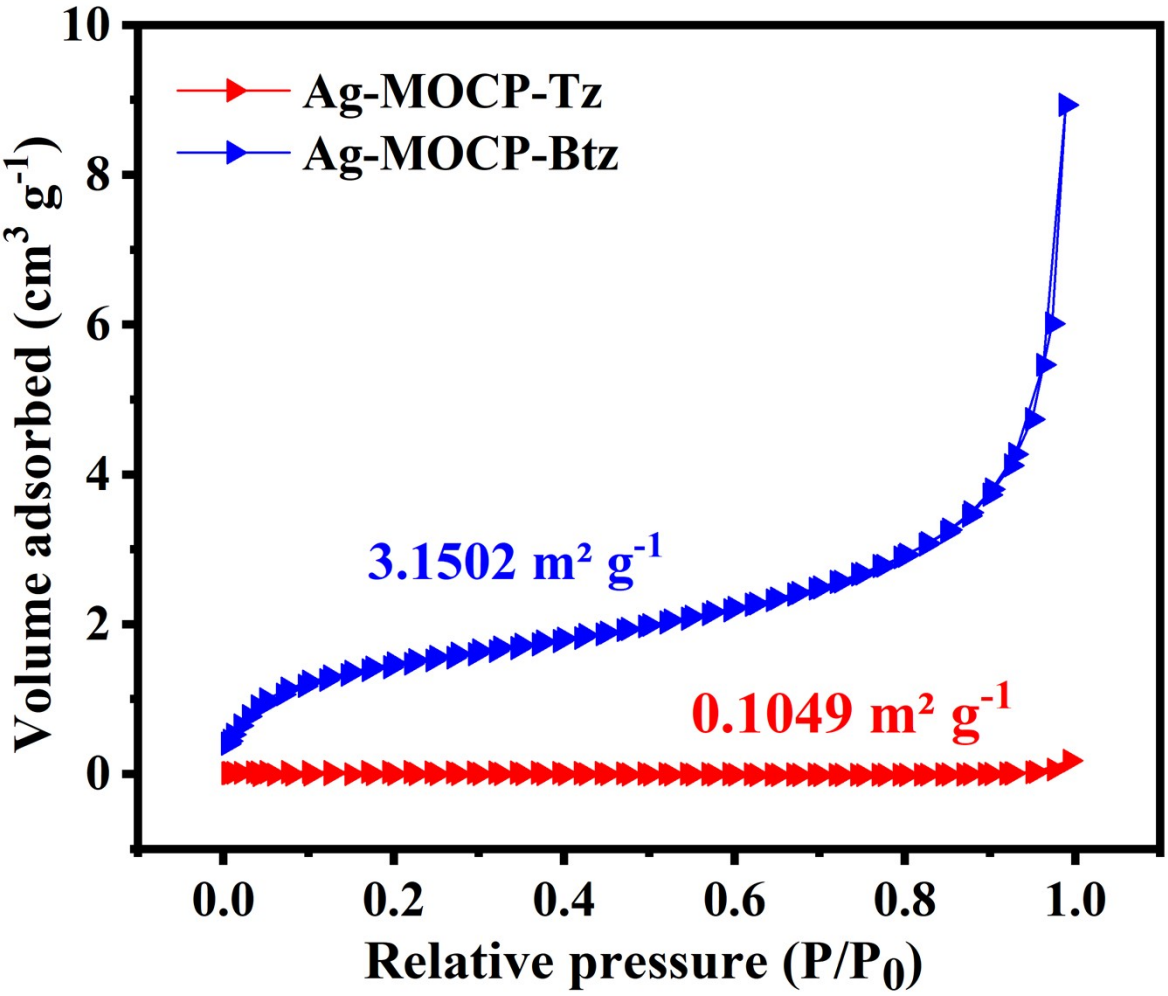

Figure S4. N_2 adsorption and desorption isotherms of Ag-MOCP-Tz and Ag-MOCP-Btz.

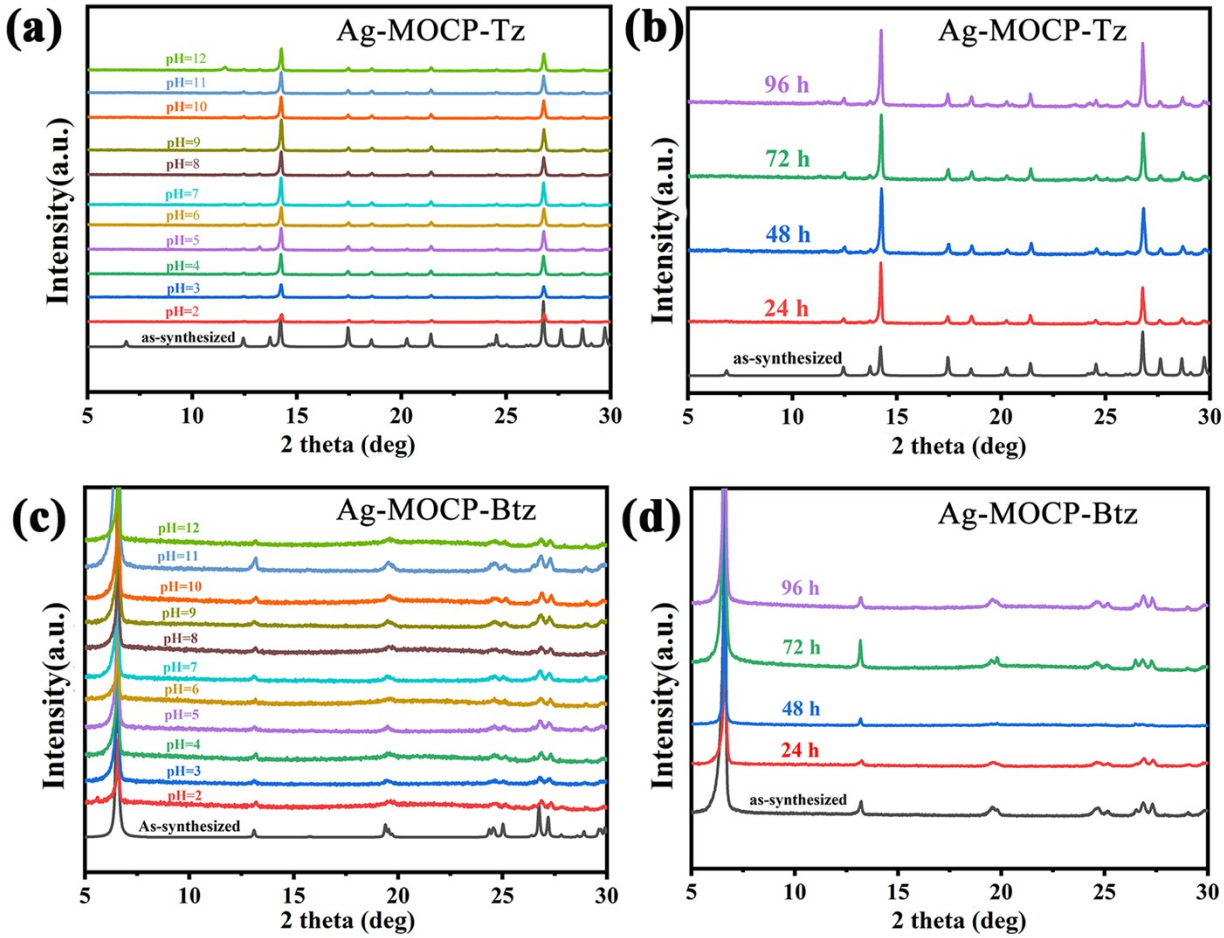

Figure S5. The powder XRD of patterns (a) different pH of Ag-MOCP-Tz, (b) in 0.5 mol L^{-1} $KHCO_3$ of Ag-MOCP-Tz, (c) different pH of Ag-MOCP-Btz, (d) in 0.5 mol L^{-1} $KHCO_3$ of Ag-MOCP-Btz.

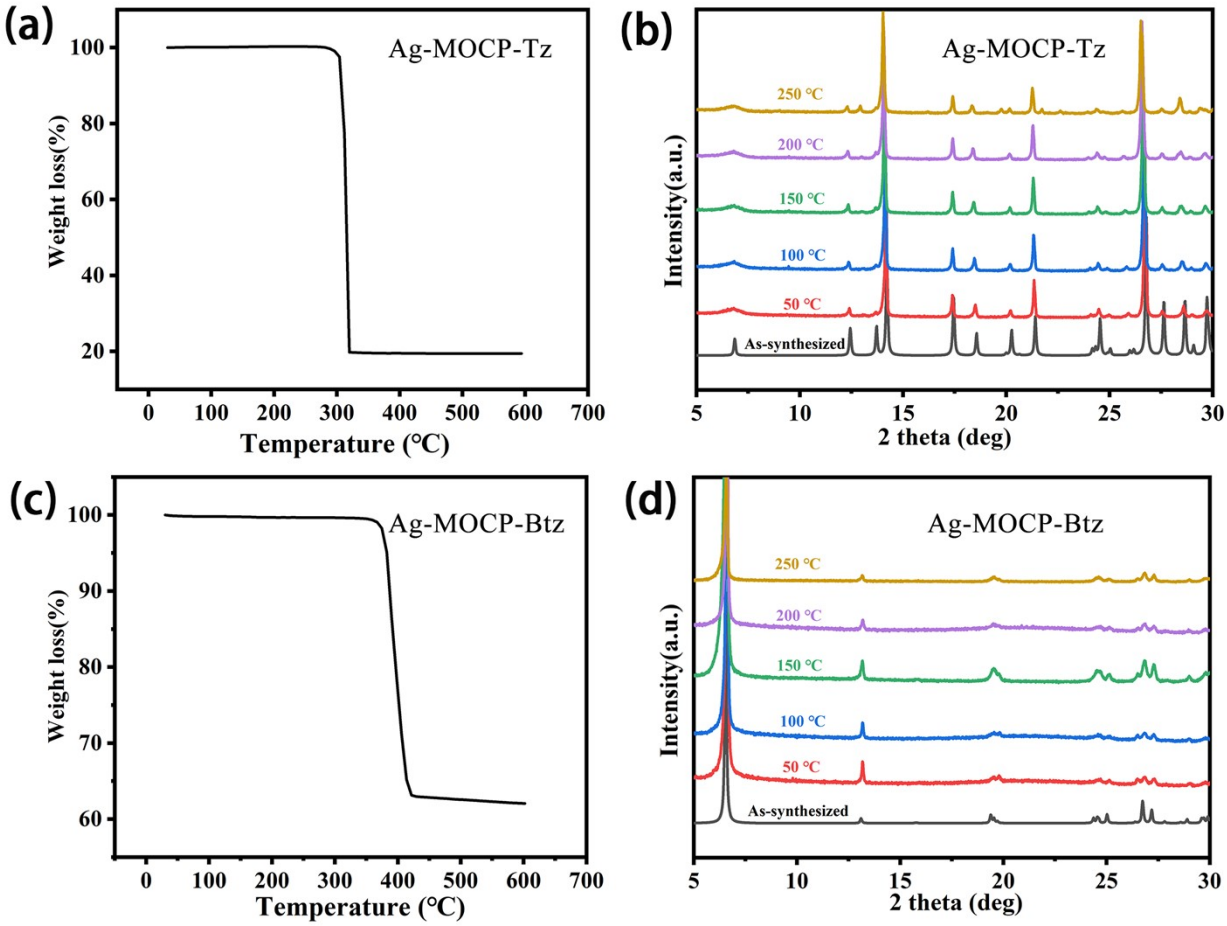

Figure S6. TGA curves of (a) Ag-MOCP-Tz and (c) Ag-MOCP-Btz; In-situ variable temperature powder XRD patterns of (a) Ag-MOCP-Tz and (c) Ag-MOCP-Btz.

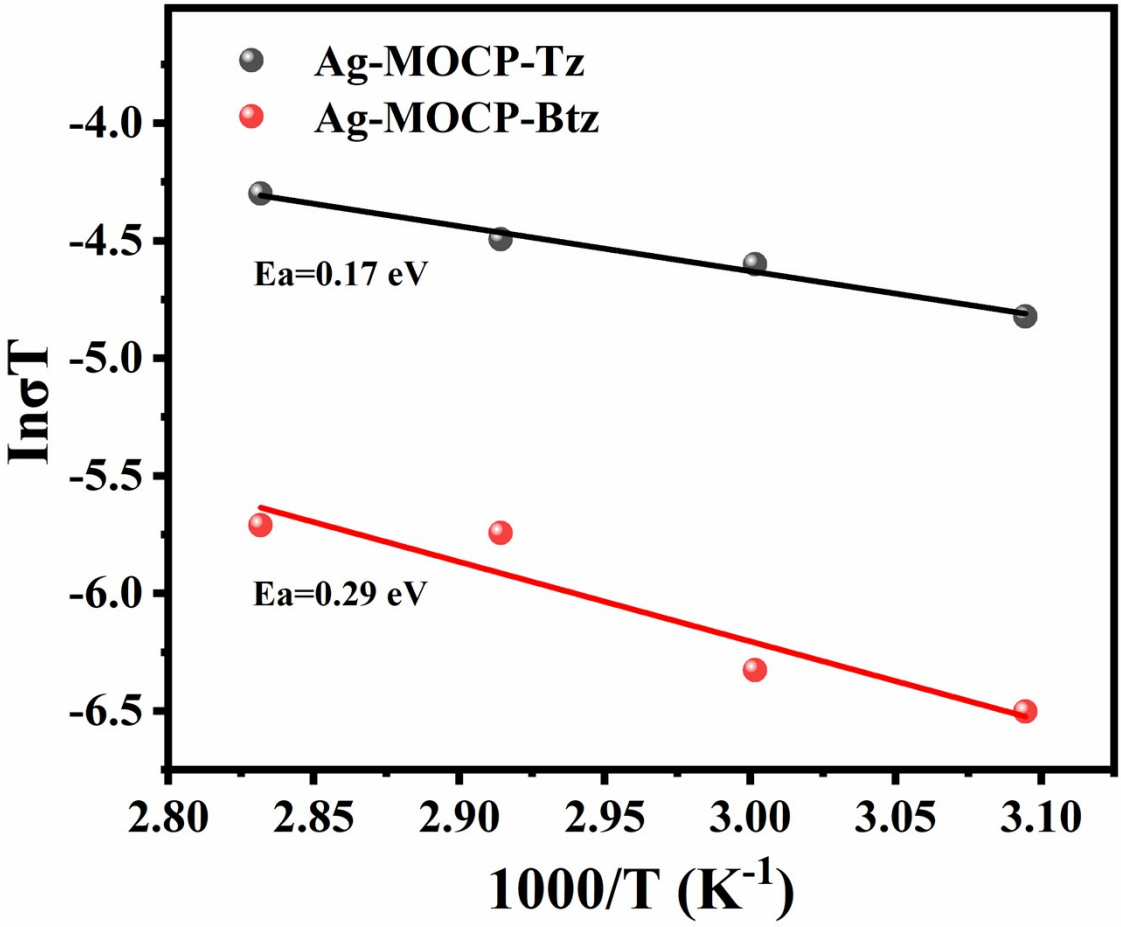

Figure S7. Arrhenius plots of Ag-MOCP-Tz and Ag-MOCP-Btz. Least-squares fitting are shown as a solid line.

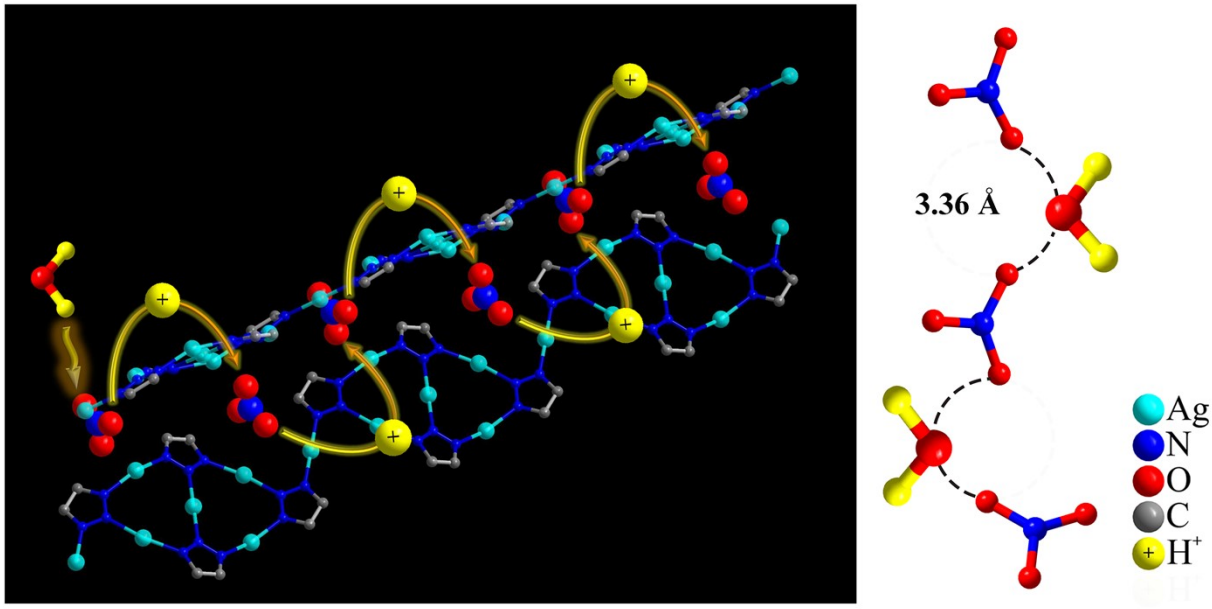

Figure S8. Schematic view of possible proton-conductive pathways in Ag-MOF-Tz.

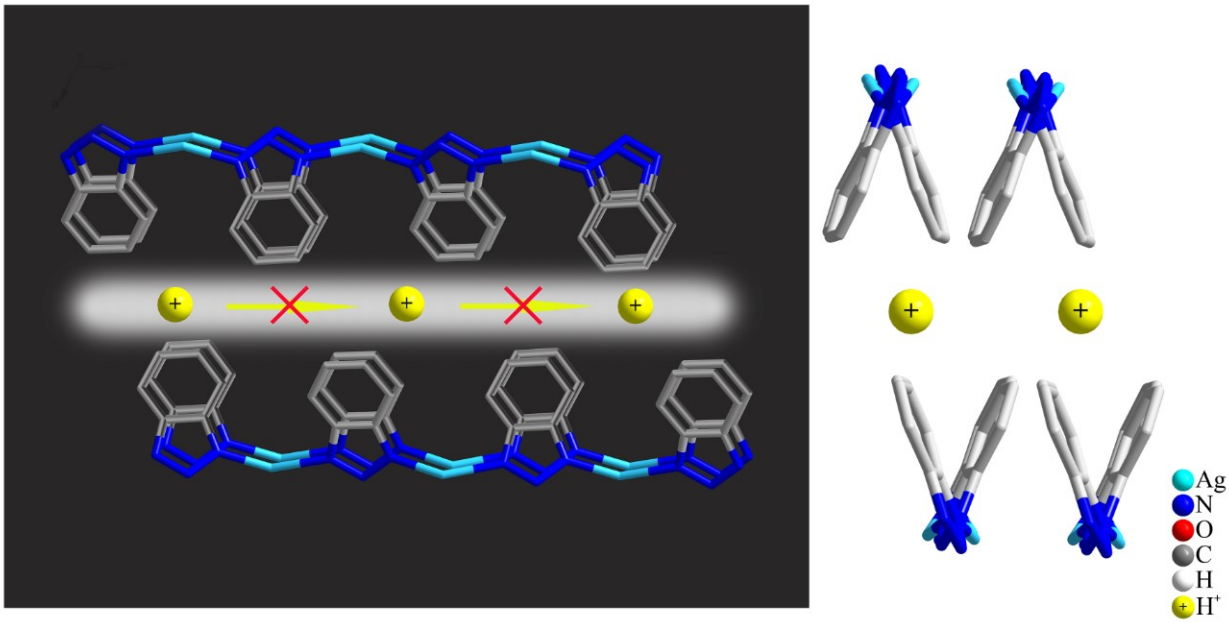

Figure S9. Schematic view of possible proton-conductive pathways in Ag-MOF-Btz.

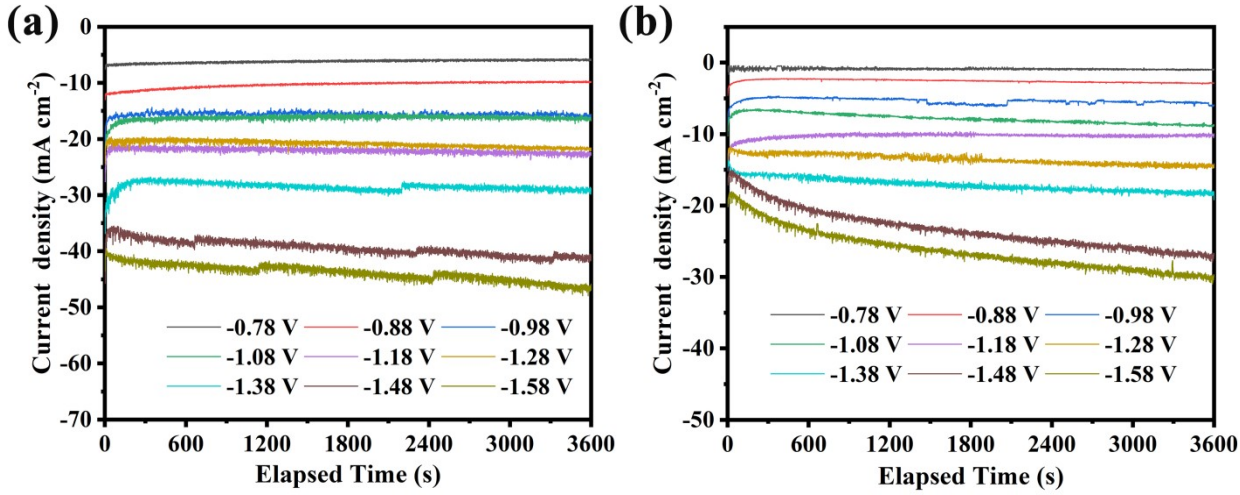

Figure S10. Current densities respect to time at given potentials for (a) Ag-MOCP-Tz and (b) Ag-MOCP-Btz.

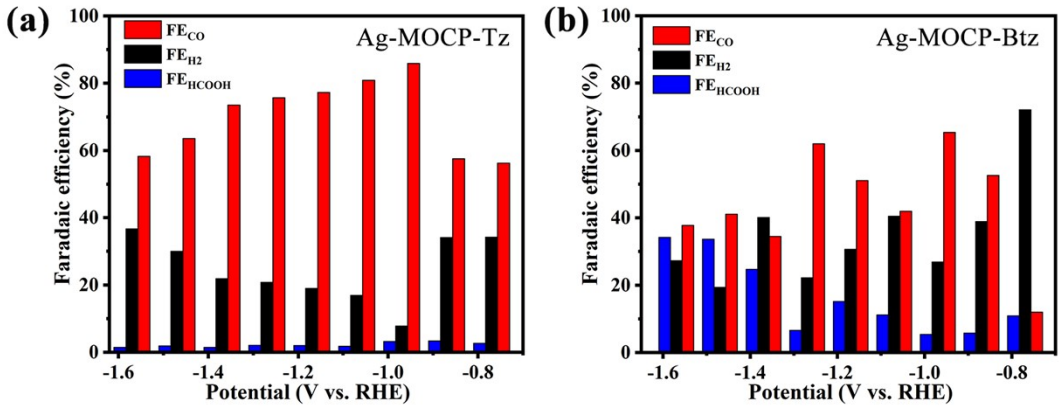

Figure S11. Potential-dependent FEs of H_2, CO and formate for (a) Ag-MOCP-Tz and (b) Ag-MOCP-Btz.

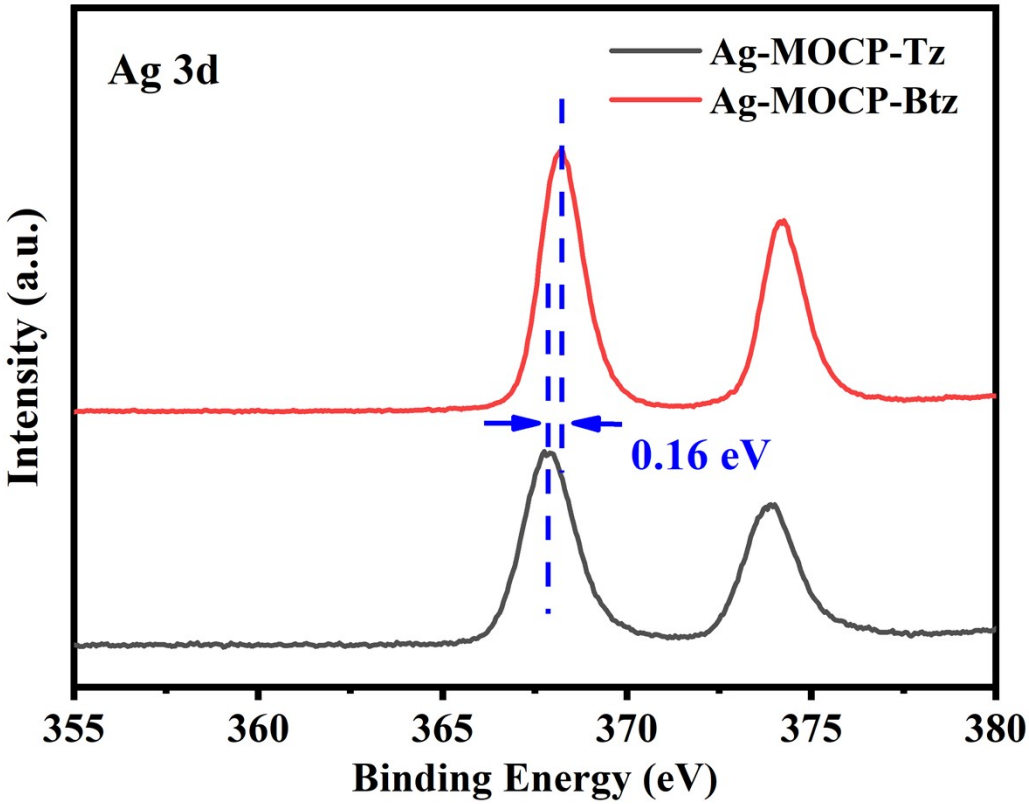

Figure S12. Ag 3d XPS spectra of Ag-MOCP-Tz and Ag-MOCP-Btz.

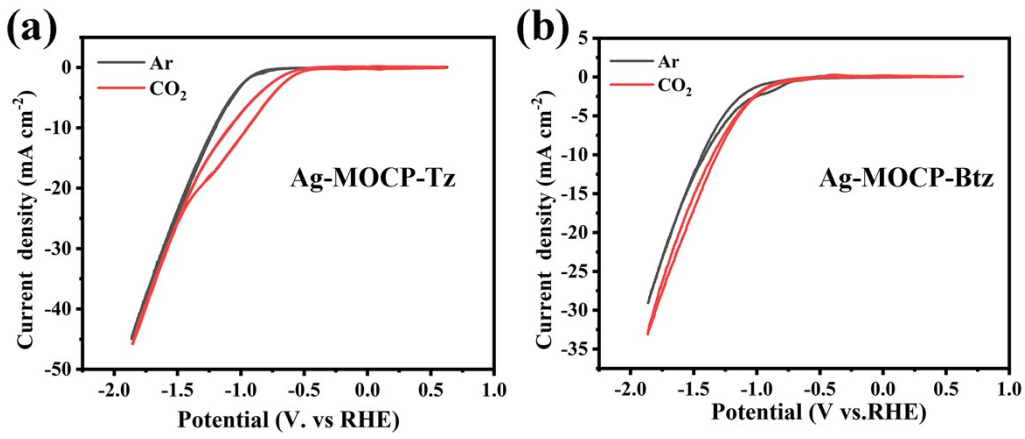

Figure S13. Cyclic voltammetry (CV) curves at a scan rate of 50 mV s^{-1} in Ar and CO_2-saturated 0.5 mol L^{-1} $KHCO_3$ solutions of Ag-MOCP-Tz and Ag-MOCP-Btz.

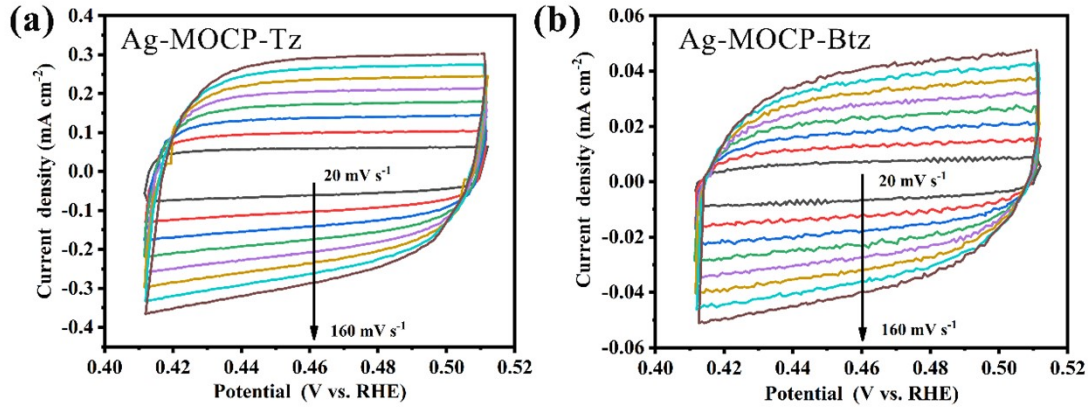

Figure S14. ECSA measurements for Ag-MOCP-Tz and Ag-MOCP-Btz (a) and (b) CV curves at different scan rates.

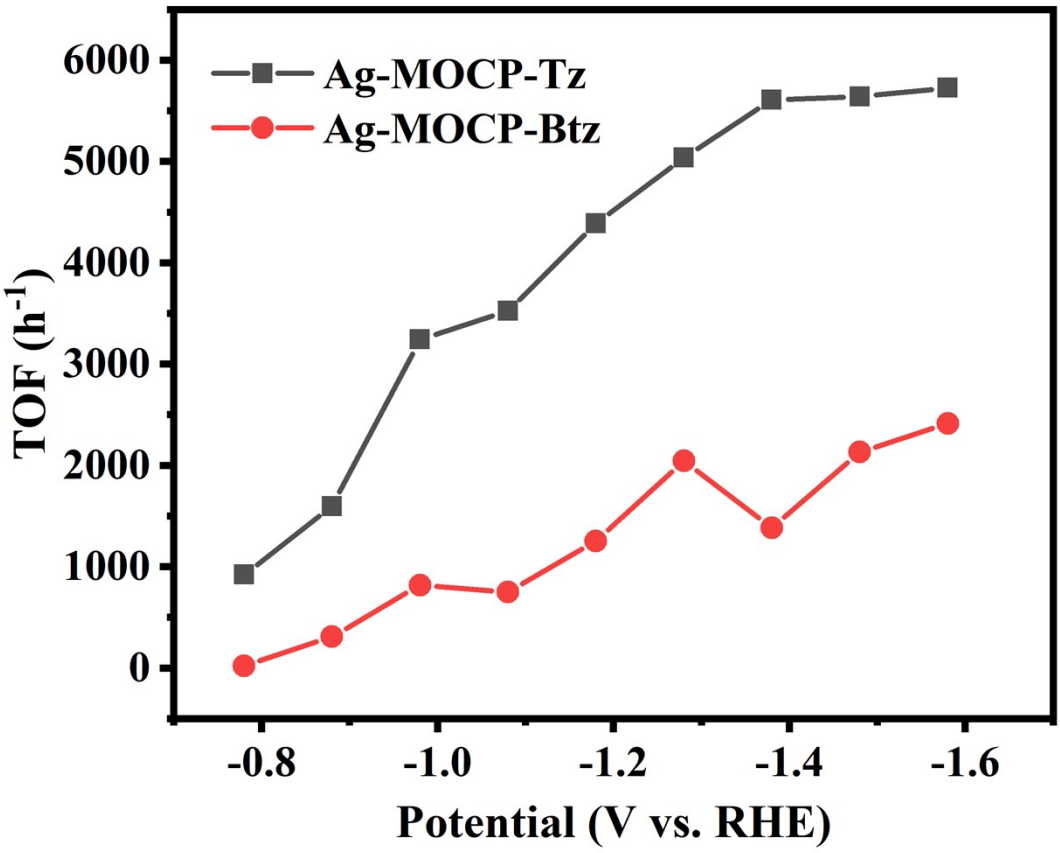

Figure S15. TOF plots of Ag-MOCP-Tz and Ag-MOCP-Btz for the generation of CO.

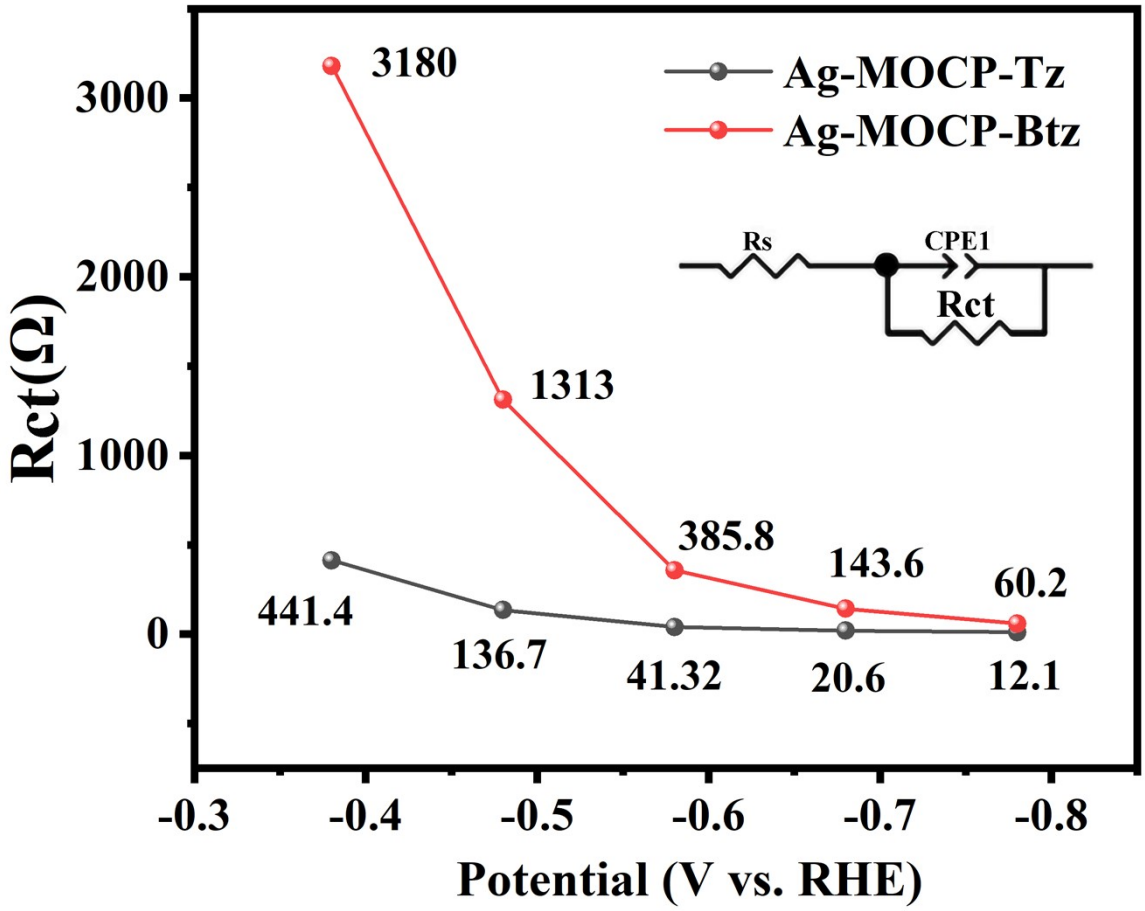

Figure S16. Rct under different potentials for Ag-MOCP-Tz and Ag-MOCP-Btz.

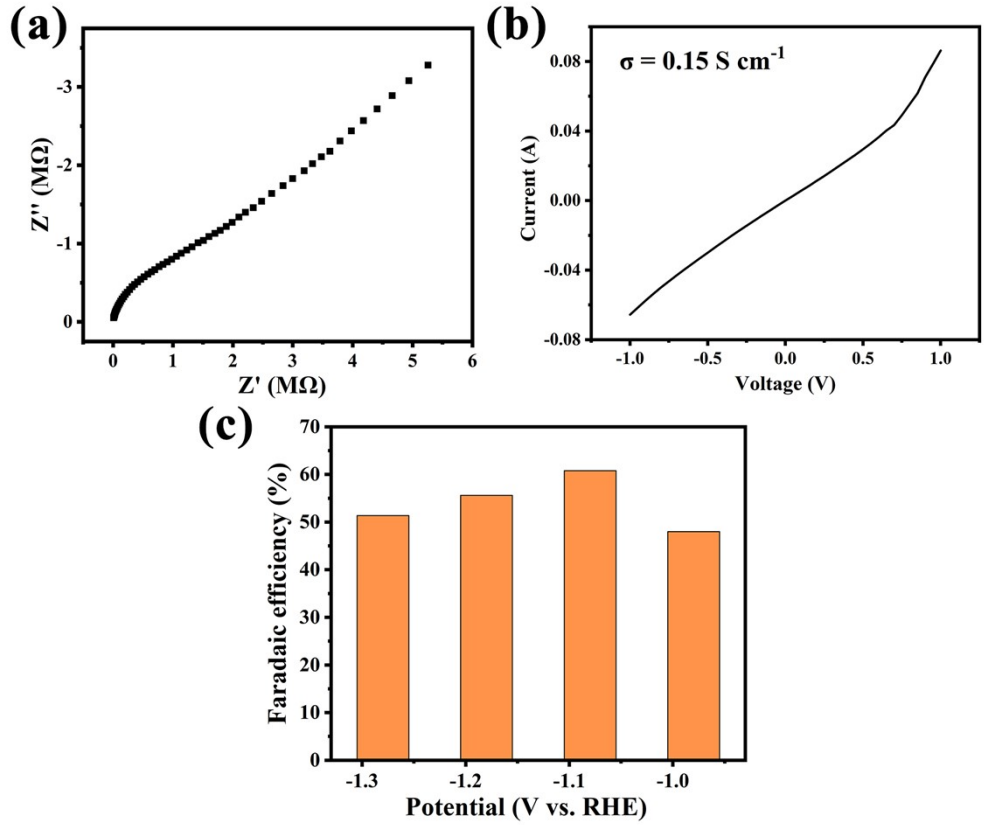

Figure S17. (a) Nyquist plots from AC impedance data of silver particles, (b) I-V curves of Ag power at room temperature, (c) the CO product distribution for CO_2RR at different potentials of Ag power.

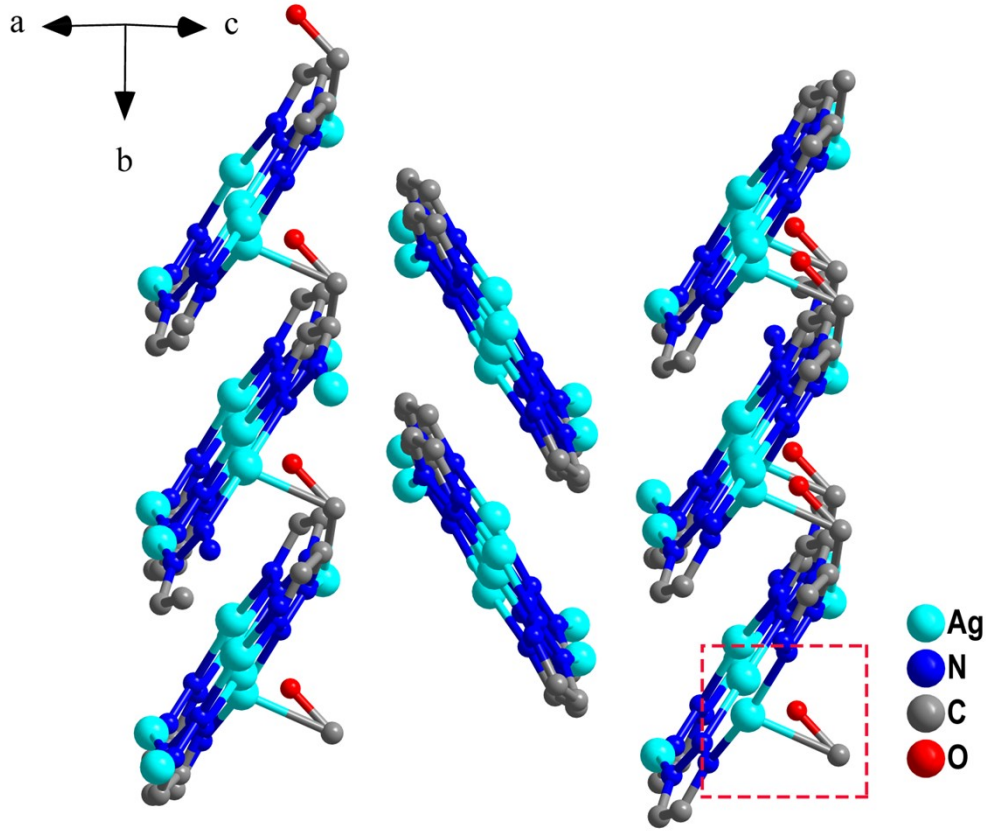

Figure S18. The noncovalent-interaction (NCI) between *CO and Ag site of Ag-MOCP-Tz.

Table S1. Crystal data and structure refinement for Ag-MOCP-Tz and Ag-MOCP-Btz.

	Ag-MOCP-Tz	**Ag-MOCP-Btz**
CCDC	2069516	293247
Crystal system	Monoclinic	Monoclinic
Space group	$P2_1/a$	$P2_1/c$
a/Å	14.271(3)	14.8052(3)
b/Å	5.5621(8)	3.7498(4)
c/Å	14.732(2)	12.3495(12)
α/°	90	90
β/	118.85(2)	114.200(5)
γ/°	90	90
Volume/Å^3	1020.4(3)	625.3(5)
Z	4	4
ρ_{calc}g/cm^3	3.396	2.459
F(000)	968.0	432
Radiation	Mo Kα (λ = 0.710)	
Goodness-of-fit on F^2	1.050	
Final R indexes [all data][(a)]	R1 = 0.0774, wR2 = 0.1367	

$R_1=\Sigma(||F_0|-|F_C||)/\Sigma|F_0|$;$wR_2 = [\Sigma w(|F_0|^2-|F_C|^2)^2/\Sigma w(F_0^2)^2]^{1/2}$.

Table S2. The performance of different MOCPs and their CO products in CO_2RR.

Catalysts	Electrolyte	FE (%)	Potential (V)	j_{co} (mA cm^{-2})	Stability (h)	Refs.
ZIF-8	0.5 M NaCl	63	-1.8 V vs. SCE	-1.6	4	6
ZIF-8	0.25 M K_2SO_4	81	-1.1 V vs. RHE	-6.9	NA	7
cobalt-porphyrin MOF	0.5 M K_2CO_3	76	-0.7 V vs. RHE	NA	7	8
CCG/CoPc-A	0.1 M $KHCO_3$	77	-0.59 V vs. RHE	NA	30	9
Fe-MOF-525/FTO	1 M $TBAPF_6$	54	-1.3 V vs. NHE	-3.2	4	10
Re-SURMOF/FTO	acetonitrile solution with 5%Vol ethanol	93	-1.6 V vs. NHE	-2.3	2	11
Co-PMOF	0.5 M $KHCO_3$	98.7	-0.8 V vs. RHE	NA	36	4
PcCu-O8-Zn	0.1 M $KHCO_3$	88	-0.7 V vs. RHE	-1.5	10	5
Cu-THQ	1 M KOH	91	-0.45 V vs. RHE	-173 (flow cell)	7	12
Ag-MOCP-Tz	0.5 M $KHCO_3$	85.9	-0.98 V vs. RHE	**-14**	**20**	**This work**
Ag-MOCP-Btz		65.4	-0.98 V vs. RHE	**-3.2**	/	

"NA" means "not available"

References

1. M. Rajeswaran, T. N. Blanton, D. J. Giesen, D. R. Whitcomb, N. Zumbulyadis, B. J. Antalek, M. M. Neumann and S. T. Misture, *J. Solid State Chem.*, 2006, **179**, 1053-1059.
2. D.-D. Ma, S.-G. Han, C. Cao, W. Wei, X. Li, B. Chen, X.-T. Wu and Q.-L. Zhu, Energy & Environmental Science, 2021, 14, 1544-1552.
3. C. Cao, D. D. Ma, J. F. Gu, X. Xie, G. Zeng, X. Li, S. G. Han, Q. L. Zhu, X. T. Wu and Q. Xu, *Angew. Chem. Int. Ed. Engl.*, 2020, **59**, 15014-15020.
4. Y. R. Wang, Q. Huang, C. T. He, Y. f. Chen, J. Liu, F. C. Shen and Y. Q. Lan, *Nat Commun*, 2018, **9**, 1-8.
5. H. Zhong, M. Ghorbani-Asl, K. H. Ly, J. Zhang, J. Ge, M. Wang, Z. Liao, D. Makarov, E. Zschech, E. Brunner, I. M. Weidinger, J. Zhang, A. V. Krasheninnikov, S. Kaskel, R. Dong and X. Feng, *Nat. Commun.*, 2020, **11**, 1-10.
6. Y. Wang, P. Hou, Z. Wang and P. Kang, *Chemphyschem*, 2017, **18**, 3142-3147.
7. X. Jiang, H. Li, J. Xiao, D. Gao, R. Si, F. Yang, Y. Li, G. Wang and X. Bao, *Nano Energy*, 2018, **52**, 345-350.
8. N. Kornienko, Y. Zhao, C. S. Kley, C. Zhu, D. Kim, S. Lin, C. J. Chang, O. M. Yaghi and P. Yang, *J. Am. Chem. Soc.*, 2015, **137**, 14129-14135.
9. J. Choi, P. Wagner, S. Gambhir, R. Jalili, D. R. MacFarlane, G. G. Wallace and D. L. Officer, *ACS Energy Letters*, 2019, **4**, 666-672.
10. I. Hod, M. D. Sampson, P. Deria, C. P. Kubiak, O. K. Farha and J. T. Hupp, *ACS. Catal.*, 2015, **5**, 6302-6309.
11. L. Ye, J. Liu, Y. Gao, C. Gong, M. Addicoat, T. Heine, C. Wöll and L. Sun, *J. Mater. Chem.*, 2016, **4**, 15320-15326.
12. L. Majidi, A. Ahmadiparidari, N. Shan, S. N. Misal, K. Kumar, Z. Huang, S. Rastegar, Z. Hemmat, X. Zou, P. Zapol, J. Cabana, L. A. Curtiss and A. Salehi-Khojin, *Adv. Mater.*, 2021, DOI: 10.1002/adma.202004393, 2004393.